

Lawrence Berkeley National Laboratory

LBL Publications

Title

Understanding the formation of polytypism in natural moissanite with Laue microdiffraction

Permalink

<https://escholarship.org/uc/item/9bv2f9c3>

Journal

Acta Crystallographica Section A: Foundations and advances, 74(a1)

ISSN

0108-7673

Authors

Stan, Camelia
O'Bannon, Earl
Dobrzhinetskaya, Larissa
et al.

Publication Date

2018-07-20

DOI

10.1107/s0108767318098264

Peer reviewed

1

1 *article*2 **X-ray Laue microdiffraction and Raman spectroscopic**
3 **investigation of silicon and moissanite from natural rocks**4 **Camelia Veronica Stan^{1*}, Earl Francis O'Bannon III^{2*}, Pavel Mukhin³, Nobumichi**
5 **Tamura⁴, and Larissa Dobrzhinetskaya⁵**6 ¹ NIF & Photon Science Directorate, Lawrence Livermore National Laboratory, PO Box 808, Livermore, California
7 94551; stan2@llnl.gov8 ² Physics and Life Science Directorate, Lawrence Livermore National Laboratory, PO Box 808, Livermore, California
9 94551; obannon2@llnl.gov10 ³ Independent Consultant in Ore Deposits, Tel Aviv, Israel11 ⁴ Advanced Light Source, Lawrence Berkeley National Laboratory, 1 Cyclotron Road, Berkeley, California, 94720;
12 ntamura@lbl.gov13 ⁵ Earth and Planetary Sciences, University of California Riverside, 900 University Avenue, Riverside, California,
14 92521; larissa@ucr.edu

15 * Correspondence: stan2@llnl.gov, obannon2@llnl.gov

16 Received: date; Accepted: date; Published: date

17 **Abstract:** Moissanite, SiC, is an uncommon accessory mineral that forms under low
18 oxygen fugacity. Here we analyze SiC occurred in natural sample of a Miocene tuff-
19 sandstone using synchrotron Laue microdiffraction and Raman spectroscopy, in order to
20 better understand the SiC phases and formation physics. The studied crystals of SiC
21 consist of 4H- and 6H-SiC domains, formed from either continuous growth or, in one
22 case, “amalgamated” together with native Si. The native Si is polycrystalline, with a large
23 crystal size relative to the analytical beam dimensions (> 1-2 μm). We find that the
24 “amalgamated” region shows low distortion or dislocation density in SiC, but these
25 features are comparatively high in Si. The distortion/deformation that is observed in Si
26 may have been caused by a mismatch in the coefficients of thermal expansion of the two
27 materials. Raman spectroscopic measurements are discussed in combination with our Laue
28 microdiffraction results. Our results suggest that these SiC grains likely grew from an
29 igneous melt.

30 **Keywords:** SiC, Laue diffraction, microdiffraction, natural silicon, moissanite, Si,
31 synchrotron, polymorph
32

33 **1. Introduction**

34 SiC may be the archetypal polytypic material (e.g. polymorphs only differ in the
35 stacking sequence of identical sheets or structural units) with greater than 250 known
36 synthetic polytypes, ~11 of which are reported as naturally occurring [1]. The polytypes are
37 typically described with a number that refers to the number of layers in a repeat that occur
38 along the stacking direction, and a letter that refers to the crystal system [2]. They generally
39 lie on a continuum between the wurtzite (2H) and zinc-blende (cubic) structures, depending
40 on the relative interplanar layering of Si and C. Figure 1 shows the stacking sequence of
41 three of the simplest naturally-occurring polytypes of SiC. Moissanite, the naturally
42 occurring SiC mineral, is typically considered to be either the 6H- or 15R-SiC structure
43 type. Which polytype forms under natural conditions is complicated, and currently there are

44 several well-summarized theories [3] ranging from thermodynamic, kinetic, and growth
45 considerations. Moreover, transformation from one polytype to another is thought to occur
46 by periodic slip around dislocations [4], diffusional rearrangement with the nucleation and
47 expansion of stacking faults [5], and/or changes in Si/C ratios during crystallization [6].

48 Naturally occurring moissanite (SiC) was first discovered within the impact rocks of
49 the Canyon Diablo meteor crater of Arizona [7]. Moissanite was once considered a
50 geological aberration [8]. Many synthetic routes have been reported (see review by
51 Abderrazak and Hmida [9]), with variations in the resulting crystal properties, but none
52 truly mimic geological conditions, which range from relatively low pressure (upper crust)
53 to high pressure (mid to lower mantle), high temperature and very low oxygen fugacity. For
54 more than a century natural occurrences of moissanite have been reported in the literature
55 and these reports are summarized in Lyakhovich [10] and Kaminsky [11]. However, in the
56 last two decades many more well-documented in-situ finds of natural moissanite have been
57 reported [10–38]. These reports suggest that moissanite may be a much more common
58 accessory mineral than previously thought.

59 Here we analyze naturally-occurring SiC in a tuff-sandstone, focusing on the
60 understanding of the mechanism of SiC formation, and on the intrinsic relationship between
61 SiC and Si recorded in one of the studied moissanite grains. We employ X-ray Laue
62 microdiffraction (μ XRD) and Raman spectroscopy to investigate the microstructure,
63 distortion, and phase relations in both SiC and Si.

64 **2. Materials and Methods**

65 **2.1. Sample Description**

66 The sample is a lithified tuff-sandstone (also referred to as tuffite) related to LBF
67 formation of Miocene age in the Yizre'el Valley of Kishon River, Israel. The rock includes
68 fragments of local sediments mixed with the pyroclastic material deposited during volcanic
69 eruption (e.g. Baer et al., [39]). The research sample consists of the hypidiomorphic crystals
70 of picroilmenite, magnetite and ulvospinel intermixed with eroded round crystals of quartz
71 and anorthite, all of which are cemented with secondary Ca, Fe, Mg – hydrous carbonates,
72 chlorite and serpentine (see detailed description in Dobrzhinetskaya et al., [36]). The thin
73 section used for this research is a piece of the same sample described in Dobrzhinetskaya et
74 al, [36] as tuffite, however it can be now identified more precisely as a tuff-sandstone due to
75 presence of a microfossil (Fig. 2a). The rock slide was cut by a diamond mini-saw and
76 mounted into an epoxy disc followed by polishing with corundum pastes of 50, 15 and
77 micron size with ultrasonic rinsing in distilled water after each step of polishing. The SiC
78 crystals were identified with the aid of optical microscopy and Raman spectroscopy. Three
79 grains of moissanite, labelled SiC1, SiC2 –containing native Si inclusions, and SiC3, were
80 chosen for analysis (Figure 2 a-d).

81 **2.2. Data Collection**

82 X-ray fluorescence (XRF) and μ XRD were collected at beamline 12.3.2 of the
83 Advanced Light Source at Lawrence Berkeley National Laboratory. A white light beam (5
84 – 24 keV) was focused to an area of $\sim 1 \times 1 \mu\text{m}^2$ using Kirkpatrick-Baez mirrors. The
85 sample was placed onto a high-precision translational stage at 45° relative to the incident
86 beam and raster scanned. XRF data was collected using a Vortex-EM XRF detector at a 20
87 \times 20 μm resolution. Scanning was performed at a rate of 0.5s / pixel. The emission lines of
88 Cr, Fe, Ni, Ca, and Ti were used to determine crystal grain locations. Since the XRF
89 detector is only sensitive in the 2000-20,000 eV range, Si ($K\alpha = 1740 \text{ eV}$) and C ($K\alpha = 277$

90 eV) cannot directly be detected, so the SiC location was determined via the absence of
91 signal.

92 Microdiffraction mapping was performed on SiC 1, SiC 2 and SiC 3 grains (Table 1),
93 allowing some margin around each crystal to account for the penetration depth of the beam
94 (~100 μm in SiC) and the 45° geometry of the sample relative to the incident beam. Data
95 was collected in 90° geometry by a Pilatus 1M detector using a 0.5 s exposure time. The
96 sample-to-detector distance was calibrated using an unstrained synthetic Si sample. Further
97 information about the experimental setup can be found in Kunz et al. [40] and Stan et al.
98 [41]. μXRD data analysis of was performed using XMAS [40,42]. Analysis of the maps
99 was performed using the supercomputing facilities at the National Energy Research
100 Scientific Computing Center (NERSC).

101 Raman maps of the Si inclusion in SiC2 were collected on a Horiba LabRam
102 Evolution Raman spectrometer with a spectrometer focal length of 800 mm. Spectra were
103 collected from 450-900 cm^{-1} and the colors were assigned based on the first order Raman
104 mode of Si and the manifold of TO modes for 4H- and 6H-SiC centered near 775 cm^{-1} .
105 Spectra were collected in a backscattered geometry with an excitation wavelength of 532
106 nm and a 1800 lines/mm grating, which results in a spectral resolution of $\sim 1 \text{ cm}^{-1}$. An
107 Olympus BXFM-ILHS microscope with a 50x long working distance objective was used to
108 focus the laser beam to a $\sim 2 \mu\text{m}$ spot size onto the sample. Maps were collected using a 2
109 μm step size. A synthetic, unstrained Si chip was used to calibrate the Raman spectrometer.
110 Peaks were fit using non-linear least squares to background-subtracted pseudo-Voigt or
111 Gaussian line profiles using the program Igor Pro.

112 3. Results

113 Three grains of SiC (size $\sim 0.5 - 1 \text{ mm}$) were chosen for detailed studies. XRF
114 measurements corresponded well with the known shape and dimensions of each grain as
115 expected from optical microscope images of the sample (Figure 2).

116 3.1. SiC1

117 Initial μXRD measurements indicates that the sample consists of a strongly diffracting single crystal.
118 Initial indexing attempts focused on the 4H-SiC polytype, which we anticipated based on previous TEM and
119 Raman spectroscopic work [36]. Most of the scanned area could be indexed as either 4H- or 6H-SiC, with
120 more than 30 peaks indexed for both polytypes (Figure 3). It is expected in general that 6H-SiC would have
121 more diffraction peaks than 4H-SiC over the same angular range, due to the difference in the c-axis length
122 between the two phases. This can easily be seen in the relative number of indexed peaks (Figure 3 a,b).

123 The grain contains an area of overlap where both unit cells can be indexed (Figures 3,4). On the left-
124 hand side of the grain, all observed peaks can be indexed as 4H-SiC only (Figure 4a), whereas on the right-
125 hand side, all peaks can be indexed as 4H-SiC only (Figure 4 c). In the center, the diffraction pattern contains
126 peaks from both, and both can be indexed, with some peaks overlapping for both unit cells (Figure 4, b).

127 3.2. SiC2

128 The bulk of this grain consists of a strongly diffracting single crystal that indexes as 4H-SiC (Figure 5).
129 The lower right-hand portion of the SiC2 sample contains both the region where an Si inclusion was found, as
130 well as a more poorly indexed region that is better fit as a 6H-SiC (Figure 5b). Although a second Si inclusion
131 was identified by optical microscopy and SEM, the diffraction data were of insufficient quality to index it. We
132 chose the mixed 4H/6H-SiC area for more detailed mapping and analysed it with $2 \times 2 \mu\text{m}^2$ resolution. The
133 bulk 4H-SiC crystal pattern is visible in this entire area. However, single crystal diffraction taking the form of
134 continuous lines can also be observed (Figure 6). We can fit the pattern using a 6H-SiC unit cell, which
135 provides a more accurate fit than the 4H-SiC pattern of the rest of the crystal body. This can be seen when
136 comparing Figures 6e and 6f, where all maxima can be captured with a 6H-SiC fit but only a select few
137 correspond to 4H. However, most of the grain is polycrystalline in this area, with a few discrete orientations
138 dominating (Figure 5c).

139 A native Si inclusion was initially identified by visual inspection due to differences in its reflectivity
140 relative to the surrounding SiC. This inclusion occurs within the mixed 4H-/6H-SiC region of the sample. By
141 scanning through the diffraction patterns, we find one area with broad, deformed peaks (Figure 7) that can be
142 indexed as diamond structured (Fd3m) Si. At least 3 distinct crystallographic orientations can be indexed,
143 indicating that the native Si inclusion is polycrystalline, but with large grain sizes (Figure 7 b-d). These grains
144 overlap for some part of the sample. A {113} reflection is the most intense in all three crystallites.
145 Examination of this peak, however, indicates that it is likely that many more subgrains exist, as evidenced by
146 the existence of several overlapping maxima (Figure 7 e-g). This is also indicative of plastic deformation
147 significant enough to cause a subgrain boundary formation. Although an area of only $\sim 36 \times \sim 30 \mu\text{m}$ is
148 exposed to the surface, we can track the persistence of the {113} reflection in these three main Si grains for at
149 least $340 \mu\text{m}$ horizontally and $590 \mu\text{m}$ vertically. This area of persistence is roughly coincident with where
150 6H-SiC is present, but with inhomogeneous diffraction intensity suggesting varying emplacement depths and/
151 or grain thickness in Si.

152 A Raman map of the Si inclusion is shown in Figure 8. 4H- and 6H-SiC can also be identified but were
153 not the focus of this measurement. The single Raman mode of silicon is due to the first-order Raman
154 scattering of the longitudinal optical (LO) and the transverse optical (TO) phonon modes which are
155 degenerated at the Γ -point [43]. Its room pressure and temperature position has been reported to range from
156 $519.5 \pm 0.8 \text{ cm}^{-1}$ to $523.0 \pm 1.0 \text{ cm}^{-1}$ [44–47]. The large range of reported frequencies is likely due to many factors
157 such as instrument calibration, tensile or compressive stress state of the Si sample. More recently it has been
158 shown that the Raman mode of un-stressed Si is observed between 520.5 and 520.7 cm^{-1} [43,48]. In this
159 sample, the Si Raman mode ranges from 522.3 to 525.2 cm^{-1} .

160 161 3.3. SiC3

162 Like SiC1, the SiC3 grain is made of two overlapping domains, which easily index to 4H-SiC or 6H-SiC
163 (Figure 9). The overlap region is like that of SiC1 (Figure 4), where peaks from both orientations can be
164 observed, suggesting that the two structures are intercalated. A second SiC orientation is observed on the left-
165 hand side of the grain, which visually appears to coincide with the presence of both a slight fracture in the
166 grain as well as the presence of a metal silicide inclusion [36]. The data were insufficient to determine the
167 mineral type of the silicide.

168 4. Discussion

169 4.1. Stress/strain relationships and crystal grain formation

170 The three SiC grains fall into two distinct categories, based on the spatial distribution
171 of the 4H- and 6H- unit cells. In the case of SiC1 and SiC3, there is an orientational
172 relationship between the 4H- and 6H-SiC regions, where both unit cells can be described by
173 the same orientation matrix. By traversing a sample, we can observe a 4H-SiC region, a
174 mixed region where some lattice planes are shared, and finally a 6H-SiC region. The
175 intercalation and lack of reorientation suggests that the sample is a single grain. Studies
176 suggest that the degree of hexagonality of SiC varies with the Si/C ratio (Haase et al. [6]
177 and refs contained therein). Therefore, grains with variable structure such as SiC1 and SiC3
178 could have grown from a slowly cooling Si/C liquidus slightly enriched in Si, where SiC
179 growth would have led to C depletion in the liquidus and an increased Si/C ratio. In such a
180 scenario, 4H-SiC would be formed at first, and continuous grain growth would lead to a
181 less hexagonal (containing some cubic ABC stacking planes) structure over time as the
182 surrounding liquidus changed, explaining the transition region between the two crystal
183 types and the final 6H-SiC structure.

184 In the case of SiC2, there is no such relationship in the orientation of 4H-SiC and 6H-
185 SiC, nor between SiC and Si. It is more likely that the 4H-SiC grain, which is visible in the
186 diffraction patterns where 6H-SiC is also present, formed independently during different
187 melting events from the 6H-SiC, and that these single crystals became “amalgamated”
188 together by remaining liquidus Si at a later time.

189 The differential stress and strain in both SiC and Si were calculated from the indexed
190 Laue diffraction map. In the 4H-SiC region, the stress/strain across the crystal was
191 homogeneous for a given tensor, so we focus the discussion mainly on the part of the map
192 that covers the exposed Si region and the entire 6H-SiC region. The strain in this area for
193 all 3 crystal types is presented in Figure 10a-c. The overall strain in the 4H-SiC region of
194 the sample is low, except for some tensile differential strain in the z direction of the sample;
195 this observation may be due to release of pressure as a result of cutting and polishing the
196 sample. The Si is under compressive differential strain in the XY plane and tensile
197 differential strain in the Z direction. The strain state seems not to depend on
198 crystallographic orientation for any of the 3 phases.

199 A possible explanation for this may be that greater plastic deformation and differential
200 strain in Si is due to a differential in the coefficient of thermal expansion (CTE) for the two
201 materials, where SiC = 4.36×10^{-6} /K (Li & Bradt, 1986) and Si = 2.63×10^{-6} /K (Watanabe
202 et al., 2004). In prior studies of dislocation generation between materials with contrasting
203 CTE, it was found that dislocation density increased relative to the pure materials when
204 subjected to similar temperature conditions [49,50]. We assume that the Si inclusion
205 formed while the sample was at high temperature which is reasonable as this SiC sample
206 likely formed at a depth of 60-100 km (~ 2 GPa) and a temperature range of 1000 – 1600
207 °C [36]. Then the factor of ~2 differences in their CTE is likely the cause of the higher
208 dislocation densities associated with the Si and SiC in the 6H-SiC region. In essence, SiC
209 would contract at a faster rate than Si, leading to greater strain in the Si. We map the
210 dislocation densities in both, assuming a {001}<110> slip system in SiC (Figure 11). This
211 assumption is borne out by the presence of diffraction “lines” in the single-crystal Laue
212 diffraction of SiC, which are indicative of stacking faults and are direct evidence of the
213 activation of this slip system. Overall, Si displays a much greater density of dislocations
214 than SiC. This is supported by observations in the diffraction, which suggest that the Si is
215 under more plastic deformation at every point where both are present.

216 4.2. SiC/Si relationship

217 One of the goals of our study was to understand the formation of a native silicon
218 inclusion such as that found in SiC₂, which requires extremely reducing conditions of
219 formation [51]. Due to the wide use of silicon in the semiconductor industry the effects of
220 tensile and compressive stresses, hydrostatic pressure, temperature, and polishing on the
221 first order Raman mode position and width are well characterized [43,45,47,48,52–59]. It is
222 well known that tensile and compressive stress affect the Raman line by a redshift and
223 blueshift respectively [54,55]. Anastassakis et al. [52] reported a splitting of the first order
224 Raman mode of Si under uniaxial stress along the [001] or [111] direction. Thus, the
225 observed shift in the first order Raman mode of our Si inclusion (Figure 8a) may be
226 evidence of residual compressive stress. Most of the grain shows a shift of ~ 1.5-2.7 cm⁻¹
227 (Figure 7a) from the ambient pressure value of 520.7 cm⁻¹. Taking the pressure shift of the
228 first order Si Raman mode reported by Weinstein and Piermarini (1975) this could be
229 suggesting that the Si grain is recording a residual pressure of ~0.3 – 0.5 GPa.

230 The FWHM of this peak ranges from ~4 – 9 cm⁻¹ (Figure 8b). The room pressure and
231 temperature FWHM of unstrained Si has previously been reported to range from ~3.2-7.0
232 cm⁻¹ depending on laser power [45,53,56,57]. Fitting very low intensity modes can be
233 difficult and can result in larger errors in peak position and FWHM. However, even
234 disregarding the very large and small observed FWHMs, the majority of the Raman spectra
235 of the Si inclusion have FWHM of ~ 5.5-7.7 cm⁻¹. Weinstein and Piermarini [47] report that
236 there is no appreciable change in the peak shape with applied pressure to ~ 10 GPa. Hence,

237 our observed peak widths and shapes do not unambiguously indicate that our inclusion is
238 recording any residual pressure.

239 Not surprisingly, the largest mode shifts are observed near the edge of the Si inclusion,
240 and the smallest shifts near the center of the inclusion. These shifts also correspond to
241 regions of largest FWHM and lowest intensity (Figure 8c). We also observe some
242 asymmetry to the higher wavenumber side of the observed Si Raman modes primarily in
243 the spectra collected near the edge of the Si inclusion, suggesting a uniaxial component to
244 the residual stress. This is consistent with the diffraction measurements above, where
245 plastic deformation was clearly observed as asymmetrical streaking in 3D peak shape
246 (Figure 7e-g). Furthermore, a lower Raman intensity is observed at the edges of the
247 inclusion, which can be simply explained by considering the penetration depth of the
248 Raman measurements. The penetration depth of a laser is dependent on the material
249 absorption coefficient α which is wavelength and temperature dependent, but for a constant
250 α intensity decays exponentially with depth according to the Beer-Lambert Law. For a 532
251 nm laser the penetration depth in Si is $\sim 0.7 \mu\text{m}$ [60]. The lowest intensities are from just
252 outside of where the Si inclusion is exposed to the surface, and these spectra also show
253 peaks that are from SiC (Figure 7c).

254 Nazzareni et al. [38] report natural SiC from a peralkaline syenite from the Azores.
255 They identified an Si inclusion with Raman spectroscopy and report that they observe the
256 first order Raman mode of Si to be at 519.65 cm^{-1} , and the position of the synthetic Si first
257 order Raman mode is 520.72 cm^{-1} . As discussed above and by Nazzareni et al. [38], one
258 can calculate the residual pressure of the Si inclusion using the pressure shift of the first
259 order Raman mode of Si reported by Weinstein and Piermarini [47]. In contrast to our
260 results, Nazzareni et al. [38] report that the first order Raman mode of their Si inclusion is
261 observed to be lower than the ambient pressure value suggesting that it is recording a
262 negative residual pressure. It should be noted that in the absence of a detailed compositional
263 analysis of the Si inclusion reported by Nazzareni et al. [38], one cannot rule out that the
264 negative shift could be due to impurities such as Fe which, for example, has been reported
265 in native silicon from the Luobusa Ophiolite [61]. The main difference between this study
266 and the study of Nazzareni et al. [38] is that their Si inclusion is still trapped inside the host
267 SiC₂ grain whereas ours was polished and has been exposed to the surface. Thus, our
268 observed positive shifts of the first order Si Raman mode may be because the Si inclusion
269 was exposed to the surface.

270 A considerable amount of work has been reported on subsurface damage in Si due to
271 polishing and grinding [59,62]. It is possible that our observed shift in the first order Si
272 Raman mode is a result of damage caused during sample polishing. Shifts of $\sim 1 \text{ cm}^{-1}$ are
273 observed in the core of the exposed Si inclusion while larger shifts are observed at the edge
274 of the exposed inclusion. Zhang et al. [59] report that the position of the first order Si
275 Raman mode for several Si wafers that were polished with different grain sizes ranging
276 from $\sim 70 - \sim 4 \mu\text{m}$. The ground wafer surfaces mainly present compressive states that are
277 dependent on the grain sized used for polishing and shifts up to 4 cm^{-1} from the ambient
278 value are observed. They find that the main reasons for the generation of residual stresses is
279 due to phase transitions. Zarudi and Zhang [62] discuss subsurface damage of single-crystal
280 silicon due to grinding and polishing. They show that the depth of damage is related to the
281 particle size of the abrasives used, and that the damage can be removed with polishing
282 (about 10 hours). Phase transitions to α -Si, Si-III, and Si-XII are also observed in polished
283 Si samples and the phases that are observed is dependent on the grain size of the polish that
284 was used [59]. We do not observe any peaks from α -Si, Si-III, or Si-XII in our spectra. The
285 stress regime in the near-surface environment of the polished and exposed Si inclusion isn't

286 simple, and likely grades from mostly compressive near the edges to more tensile in the
287 middle. It is difficult to deconvolve the signals from (1) actual residual pressure that may be
288 recorded by the grain due to thermal expansion differences, (2) artefacts from polishing the
289 sample, and (3) the exposure of the Si inclusion to the surface on one side. To verify these
290 statements, the additional experiments are necessary to conduct by recording Raman
291 spectra of the synthetic Si crystals before and after polishing.

292 5. Conclusions

293 The XRF, μ XRD, and Raman spectroscopy studies of 3 grain of natural SiC suggest
294 that each of them consist of two polytypes of SiC, 4H- and 6-SiC. These SiC polytypes
295 were found to be either intergrown during a single growth event (SiC1 and SiC3), or
296 “amalgamated/cemented” together after the initial formation of SiC crystals (SiC2) with
297 polycrystalline, more deformed Si. There is no straightforward explanation for which SiC
298 polytype will form first, and current theories include impurity arguments, kinetic and
299 growth considerations, and thermodynamics. In a natural system the liquid will have a
300 particular Si/C ratio as well as some quantity of impurities. This liquid will cool at some
301 rate and a certain SiC polytype will crystallize. Since we observe both 4H- and 6H-SiC, and
302 if we assume a closed system crystallization of SiC, crystal growth will change the Si/C
303 ratio. It has been proposed that the Si/C ratio will determine which polytype will form [6].
304 This hypothesis was invoked to explain the natural zoned SiC that was found in
305 metamorphic rocks from Bulgaria [37]. Thus, we propose that for SiC 1 and SiC 3 one
306 nucleation event led to grain formation through a change in the Si/C ratio, likely caused by
307 C depletion during grain growth, and in the case of SiC 2 two different nucleation events
308 likely occurred.

309 Despite its high hardness, SiC deforms plastically and polygonizes at high temperature
310 [63]. Dislocations in (0001), dislocations with [11-20] vectors, and pileups formed by slip
311 and dislocation walls formed by climb were all reported by Amelinckx et al. [63].
312 Dislocations in microdiamonds have also been reported [64,65]. Kvasnytsya and Wirth [65]
313 report a high density of curved dislocations in one of their microdiamond samples from a
314 meteorite impact area, and suggest a thermally activated process where the diamond
315 experienced a period of thermal annealing after deformation. Dobrzhinetskaya et al. [64]
316 found dislocations in microdiamonds from ultra-high pressure metamorphic terranes and
317 assigned them to dislocations of growth, e.g. during nucleation process the volume may
318 have been under differential stress. The observed low dislocation density in the examined
319 SiC crystals suggests that the samples may not have remained at high temperatures for an
320 extended period of time, nor did they undergo any high temperature deformation at any
321 time after their initial crystallization. While these new results still cannot place any
322 constraint on the depth of formation of these grains, they do support their high-temperature
323 origin which was reported earlier by Dobrzhinetskaya et al. [36]. Given the wide stability
324 field of SiC, from the shallow mantle to the deep Earth, one should be cautious when
325 interpreting formation conditions of natural SiC.

326 **Author Contributions:** CVS, EFO: data collection and interpretation, writing and editing. NT: data collection and
327 interpretation. PM: resources and sample preparation. LD: conception, data interpretation, writing and editing. All authors
328 have read and agreed to the published version of the manuscript.

329 **Funding:** EFO was partially supported by NSF through EAR-1620423. A portion of this work was performed under the
330 auspices of the US Department of Energy by Lawrence Livermore National Laboratory under Contract No. DE-AC52-
331 07NA27344. This research used resources of the National Energy Research Scientific Computing Center, a DOE Office of
332 Science User Facility supported by the Office of Science of the U.S. Department of Energy under Contract No. DE-AC02-
333 05CH11231. The Advanced Light Source is supported by the Director, Office of Science, Office of Basic Energy

334 Sciences, Materials Sciences Division, of the U.S. Department of Energy under Contract No. DE-AC02-05CH11231 at
335 Lawrence Berkeley National Laboratory and University of California, Berkeley, California.

336 **Conflicts of Interest:** The authors declare no conflict of interest.

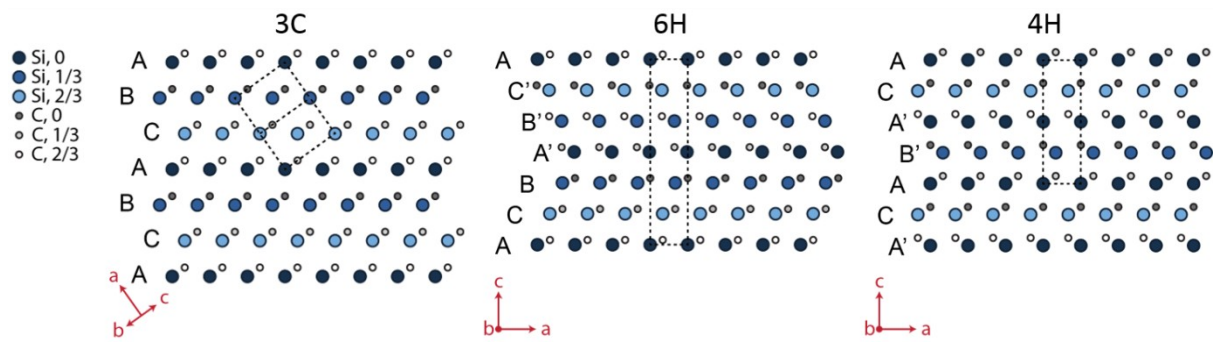
337 **References**

- 338 1. Cheung, R. *Silicon Carbide Microelectromechanical Systems for Harsh Environments*; Imperial College Press:
339 London, UK, 2006; ISBN 978-1-86094-624-0.
- 340 2. Ramsdell, L.S. Studies on silicon carbide. *Am. Mineral.* **1947**, *32*, 64–82.
- 341 3. Jepps, N.W.; Page, T.F. Polytypic transformations in silicon carbide. *Progress in crystal growth and*
342 *characterization* **1983**, *7*, 259–307.
- 343 4. Powell, J.A.; Will, H.A. Low-Temperature Solid-State Phase Transformations in 2H Silicon Carbide. *Journal of*
344 *Applied Physics* **1972**, *43*, 1400–1408.
- 345 5. Jagodzinski, H. Polytypism in SiC crystals. *Acta Cryst.* **1954**, *7*, 300–300.
- 346 6. Haase, V.; Kirschstein, G.; List, H.; Ruprecht, S.; Sangster, R.; Schröder, F.; Töpper, W.; Vanecek, H.; Heit, W.;
347 Schlichting, J.; et al. *Si Silicon: System Si-C. SiC: Natural Occurrence. Preparation and Manufacturing Chemistry.*
348 *Special Forms. Manufacture. Electrochemical Properties. Chemical Reactions. Applications. Ternary and Higher*
349 *Systems with Si and C*; Gmelin Handbook of Inorganic Chemistry; 1985; Vol. B3; ISBN 978-3-662-06994-3.
- 350 7. Moissan, H. Nouvelles recherches sur la météorite de Cañon Diablo. *Comptes rendus* **1904**, *139*, 773–86.
- 351 8. Milton, C.; Vitaliano, D.B. Moissanite SiC, a geological aberration. In Proceedings of the 98th Annual Meeting of
352 the Geological Society of America; 1985.
- 353 9. Abderrazak, H.; Hmida, E.S.B.H. Silicon Carbide: Synthesis and Properties. In *Properties and Applications of*
354 *Silicon Carbide*; 2011.
- 355 10. Lyakhovich, V.V. Origin of accessory moissanite. *International Geology Review* **1980**, *22*, 961–970.
- 356 11. Kaminsky, F. Mineralogy of the lower mantle: A review of ‘super-deep’ mineral inclusions in diamond. *Earth-*
357 *Science Reviews* **2012**, *110*, 127–147.
- 358 12. Ohrenschall, R.D.; Milton, C. The occurrence of moissanite (silicon carbide) in sediments. *Journal of Sedimentary*
359 *Research* **1931**, *1*, 96–99.
- 360 13. Kaminskiy, F.V.; Bukin, V.J.; Potapov, S.V.; Arkus, N.G.; Ivanova, V.G. Discoveries of silicon carbide under
361 natural conditions and their genetic importance. *International Geology Review* **1969**, *11*, 561–569.
- 362 14. Ross, J. *Kimberlites and Related Rocks*; John Wiley & Sons, Incorporated, 1989; ISBN 978-0-86793-384-0.
- 363 15. Leung, I.S. Silicon carbide cluster entrapped in a diamond from Fuxian, China. *Am. Mineral.* **1990**, *75*, 1110–1119.
- 364 16. Leung, I.; Guo, W.; Friedman, I.; Gleason, J. Natural occurrence of silicon carbide in a diamondiferous kimberlite
365 from Fuxian. *Nature* **1990**, *346*, 352.
- 366 17. Marshintsev, V.K. Nature of silicon carbide in kimberlite rocks of Yakutiya. *Mineralogicheskii Zhurnal* **1990**, *12*,
367 17–26.
- 368 18. Wilding, M.C.; Harte, B.; Harris, J.W. Evidence for a deep origin of São Luis diamonds.; 1991; pp. 456–458.
- 369 19. Svisero, D.P. Distribution and origin of diamonds in Brazil: An overview. *Journal of Geodynamics* **1995**, *20*, 493–
370 514.
- 371 20. McCammon, C.; Hutchison, M.; Harris, J. Ferric iron content of mineral inclusions in diamonds from Sao Luiz: a
372 view into the lower mantle. *Science* **1997**, *278*, 434–436.
- 373 21. Di Pierro, S.; Gnos, E.; Grobety, B.H.; Armbruster, T.; Bernasconi, S.M.; Ulmer, P. Letters. Rock-forming
374 moissanite (natural α -silicon carbide). *Am. Mineral.* **2003**, *88*, 1817–1821.
- 375 22. Zhang, Z. Native gold and native copper grains enclosed by olivine phenocrysts in a picrite lava of the Emeishan
376 large igneous province, SW China. *American Mineralogist* **2006**, *91*, 1178–1183.

- 377 23. Klein-BenDavid, O.; Wirth, R.; Navon, O. Micrometer-scale cavities in fibrous and cloudy diamonds — A glance
378 into diamond dissolution events. *Earth Planet Sc. Lett.* **2007**, *264*, 89–103.
- 379 24. Qi, X.; Yang, J.; Xu, Z.; Bai, W.; Zhang, Z.; Fang, Q. Discovery of moissanite in retrogressive eclogite from the Pre-
380 pilot Hole of the Chinese Continental Scientific Drilling Project (CCSD-PP2) and its geological implication. *Acta*
381 *Petrologica Sinica* **2007**, *23*, 3207–3214.
- 382 25. Xu, S.; Wu, W.; Xiao, W.; Yang, J.; Chen, J.; Ji, S.; Liu, Y. Moissanite in serpentinite from the Dabie Mountains in
383 China. *Mineralogical Magazine* **2008**, *72*, 899–908.
- 384 26. Lee, J.-S.; Yu, S.-C.; Tung, S.-F.; Bai, W.-J.; Yang, J.-S.; Fang, Q.-S.; Zhang, Z. The crystal structure of natural ³³R
385 moissanite from Tibet. *Zeitschrift für Kristallographie - Crystalline Materials* **2009**, *221*, 213–217.
- 386 27. Trumbull, R.B.; Yang, J.-S.; Robinson, P.T.; Di Pierro, S.; Vennemann, T.; Wiedenbeck, M. The carbon isotope
387 composition of natural SiC (moissanite) from the Earth's mantle: New discoveries from ophiolites. *Lithos* **2009**, *113*,
388 612–620.
- 389 28. Yusupov, R.G.; Stanley, C.J.; Welch, M.D.; Spratt, J.; Cressey, G.; Rumsey, M.S.; Seltsmann, R.; Igamberdiev, E.
390 Mavlyanovite, Mn₅Si₃: a new mineral species from a lamproite diatreme, Chatkal Ridge, Uzbekistan. *Mineralogical*
391 *Magazine* **2009**, *73*, 43–50.
- 392 29. Shiryayev, A.A.; Griffin, W.L.; Stoyanov, E. Moissanite (SiC) from kimberlites: Polytypes, trace elements, inclusions
393 and speculations on origin. *Lithos* **2011**, *122*, 152–164.
- 394 30. Fritsch, E.; Toledo, V.; Matlins, A. *Gems & Gemology*. Summer 2014, pp. 160–161.
- 395 31. Liang, F.; Xu, Z.; Zhao, J. In-situ Moissanite in Dunite: Deep Mantle Origin of Mantle Peridotite in Luobusa
396 Ophiolite, Tibet. *Acta Geologica Sinica - English Edition* **2014**, *88*, 517–529.
- 397 32. Liu, Y.; He, D.; Gao, C.; Foley, S.; Gao, S.; Hu, Z.; Zong, K.; Chen, H. First direct evidence of sedimentary
398 carbonate recycling in subduction-related xenoliths. *Scientific Reports* **2015**, *5*, 11547.
- 399 33. Xu, X.; Yang, J.; Robinson, P.T.; Xiong, F.; Ba, D.; Guo, G. Origin of ultrahigh pressure and highly reduced
400 minerals in podiform chromitites and associated mantle peridotites of the Luobusa ophiolite, Tibet. *Gondwana*
401 *Research* **2015**, *27*, 686–700.
- 402 34. Yang, J.; Meng, F.; Xu, X.; Robinson, P.T.; Dilek, Y.; Makeyev, A.B.; Wirth, R.; Wiedenbeck, M.; Cliff, J.
403 Diamonds, native elements and metal alloys from chromitites of the Ray-Iz ophiolite of the Polar Urals. *Gondwana*
404 *Research* **2015**, *27*, 459–485.
- 405 35. Di Pierro, S.; Gnos, E. Ca-Al-silicate inclusions in natural moissanite (SiC). *American Mineralogist* **2016**, *101*, 71–
406 81.
- 407 36. Dobrzhinetskaya, L.; Mukhin, P.; Wang, Q.; Wirth, R.; O'Bannon, E.; Zhao, W.; Eppelbaum, L.; Sokhonchuk, T.
408 Moissanite (SiC) with metal-silicide and silicon inclusions from tuff of Israel: Raman spectroscopy and electron
409 microscope studies. *Lithos* **2018**, *310–311*, 355–368.
- 410 37. Machev, P.; O'Bannon, E.F.; Bozhilov, K.N.; Wang, Q.; Dobrzhinetskaya, L. Not all moissanites are created equal:
411 New constraints on moissanite from metamorphic rocks of Bulgaria. *Earth and Planetary Science Letters* **2018**, *498*,
412 387–396.
- 413 38. Nazzareni, S.; Nestola, F.; Zanon, V.; Bindi, L.; Scricciolo, E.; Petrelli, M.; Zanatta, M.; Mariotto, G.; Giuli, G.
414 Discovery of moissanite in a peralkaline syenite from the Azores Islands. *Lithos* **2019**, *324–325*, 68–73.
- 415 39. Baer, G.; Aharon, L.; Heimann, A.; Shaliv, G.; Agnon, A. The Nahal Tavor vent: Interplay of Miocene tectonics,
416 dikes, and volcanism in the Lower Galilee, Israel. *Israel Journal of Earth Sciences* **2006**, *55*, 1–16.
- 417 40. Kunz, M.; Tamura, N.; Chen, K.; MacDowell, A.A.; Celestre, R.S.; Church, M.M.; Fakra, S.; Domning, E.E.;
418 Glossinger, J.M.; Kirschman, J.L.; et al. A dedicated superbend x-ray microdiffraction beamline for materials, geo-
419 and environmental sciences at the advanced light source. *Rev. Sci. Instrum.* **2009**, *80*, 035108.

- 420 41. Stan, C.V.; Tamura, N. Synchrotron X-ray Microdiffraction and Fluorescence Imaging of Mineral and Rock
421 Samples. *JoVE* **2018**, *in press*.
- 422 42. Tamura, N.; MacDowell, A.A.; Spolenak, R.; Valek, B.C.; Bravman, J.C.; Brown, W.L.; Celestre, R.S.; Padmore,
423 H.A.; Batterman, B.W.; Patel, J.R. Scanning X-ray microdiffraction with submicrometer white beam for strain/stress
424 and orientation mapping in thin films. *J. Synchrotron Radiat.* **2003**, *10*, 137–143.
- 425 43. Merlen, A.; Sangar, A.; Torchio, P.; Kallepalli, L.N.D.; Grojo, D.; Utéza, O.; Delaporte, P. Multi-wavelength
426 enhancement of silicon Raman scattering by nanoscale laser surface ablation. *Appl. Surf. Sci.* **2013**, *284*, 545–548.
- 427 44. Russell, J.P. Raman scattering in silicon. *Appl. Phys. Lett.* **1965**, *6*, 223–224.
- 428 45. Parker, J.H.; Feldman, D.W.; Ashkin, M. Raman Scattering by Silicon and Germanium. *Phys. Rev.* **1967**, *155*, 712–
429 714.
- 430 46. Uchinokura, K.; Sekine, T.; Matsuura, E. Raman scattering by silicon. *Solid State Communications* **1972**, *11*, 47–49.
- 431 47. Weinstein, B.A.; Piermarini, G.J. Raman scattering and phonon dispersion in Si and GaP at very high pressure. *Phys.*
432 *Rev. B* **1975**, *12*, 1172–1186.
- 433 48. Poborchii, V.; Tada, T.; Kanayama, T. Study of stress in a shallow-trench-isolated Si structure using polarized
434 confocal near-UV Raman microscopy of its cross section. *Appl. Phys. Lett.* **2007**, *91*, 241902.
- 435 49. Arsenault, R.J.; Shi, N. Dislocation generation due to differences between the coefficients of thermal expansion.
436 *Materials Science and Engineering* **1986**, *81*, 175–187.
- 437 50. Vogelsang, M.; Arsenault, R.J.; Fisher, R.M. An *in situ* HVEM study of dislocation generation at Al/SiC interfaces
438 in metal matrix composites. *MTA* **1986**, *17*, 379–389.
- 439 51. Mathez, E.A.; Fogel, R.A.; Hutcheon, I.D.; Marshintsev, V.K. Carbon isotopic composition and origin of SiC from
440 kimberlites of Yakutia, Russia. *Geochim. Cosmochim. Ac.* **1995**, *59*, 781–791.
- 441 52. Anastassakis, E.; Pinczuk, A.; Burstein, E.; Pollak, F.H.; Cardona, M. Effect of static uniaxial stress on the Raman
442 spectrum of silicon. *Solid State Commun.* **1970**, *8*, 133–138.
- 443 53. Hart, T.R.; Aggarwal, R.L.; Lax, B. Temperature Dependence of Raman Scattering in Silicon. *Phys. Rev. B* **1970**, *1*,
444 638–642.
- 445 54. Cerdeira, F.; Buchenauer, C.J.; Pollak, F.H.; Cardona, M. Stress-Induced Shifts of First-Order Raman Frequencies of
446 Diamond- and Zinc-Blende-Type Semiconductors. *Phys. Rev. B* **1972**, *5*, 580–593.
- 447 55. Campbell, I.H.; Fauchet, P.M. The effects of microcrystal size and shape on the one phonon Raman spectra of
448 crystalline semiconductors. *Solid State Communications* **1986**, *58*, 739–741.
- 449 56. Kouteva-Arguirova, S.; Arguirov, Tz.; Wolfram, D.; Reif, J. Influence of local heating on micro-Raman
450 spectroscopy of silicon. *Journal of Applied Physics* **2003**, *94*, 4946–4949.
- 451 57. Georgi, C.; Hecker, M.; Zschech, E. Effects of laser-induced heating on Raman stress measurements of silicon and
452 silicon-germanium structures. *Journal of Applied Physics* **2007**, *101*, 123104.
- 453 58. Yang, Y.; Munck, K.D.; Teixeira, R.C.; Swinnen, B.; Verlinden, B.; Wolf, I.D. Process induced sub-surface damage
454 in mechanically ground silicon wafers. *Semicond. Sci. Technol.* **2008**, *23*, 075038.
- 455 59. Zhang, Y.; Wang, D.; Gao, W.; Kang, R. Residual stress analysis on silicon wafer surface layers induced by ultra-
456 precision grinding. *Rare Metals* **2011**, *30*, 278–281.
- 457 60. Xu, Z.; He, Z.; Song, Y.; Fu, X.; Rommel, M.; Luo, X.; Hartmaier, A.; Zhang, J.; Fang, F. Topic Review:
458 Application of Raman Spectroscopy Characterization in Micro/Nano-Machining. *Micromachines* **2018**, *9*, 361.
- 459 61. Robinson, P.T.; Bai, W.-J.; Malpas, J.; Yang, J.-S.; Zhou, M.-F.; Fang, Q.-S.; Hu, X.-F.; Cameron, S.; Staudigel, H.
460 Ultra-high pressure minerals in the Luobusa Ophiolite, Tibet, and their tectonic implications. *Geological Society,*
461 *London, Special Publications* **2004**, *226*, 247–271.
- 462 62. Zarudi, I.; Zhang, L. Subsurface damage in single-crystal silicon due to grinding and polishing. *J Mater Sci Lett*
463 **1996**, *15*, 586–587.

- 464 63. Amelinckx, S.; Strumane, G.; Webb, W.W. Dislocations in Silicon Carbide. *Journal of Applied Physics* **1960**, *31*,
465 1359–1370.
- 466 64. Dobrzhinetskaya, L.F.; Green, H.W.; Bozhilov, K.N.; Mitchell, T.E.; Dickerson, R.M. Crystallization environment
467 of Kazakhstan microdiamond: evidence from nanometric inclusions and mineral associations. *Journal of*
468 *Metamorphic Geology* **2003**, *21*, 425–437.
- 469 65. Kvasnytsya, V.M.; Wirth, R. Nanoinclusions in microdiamonds from Neogenic sands of the Ukraine (Samotkan'
470 placer): A TEM study. *Lithos* **2009**, *113*, 454–464.
471



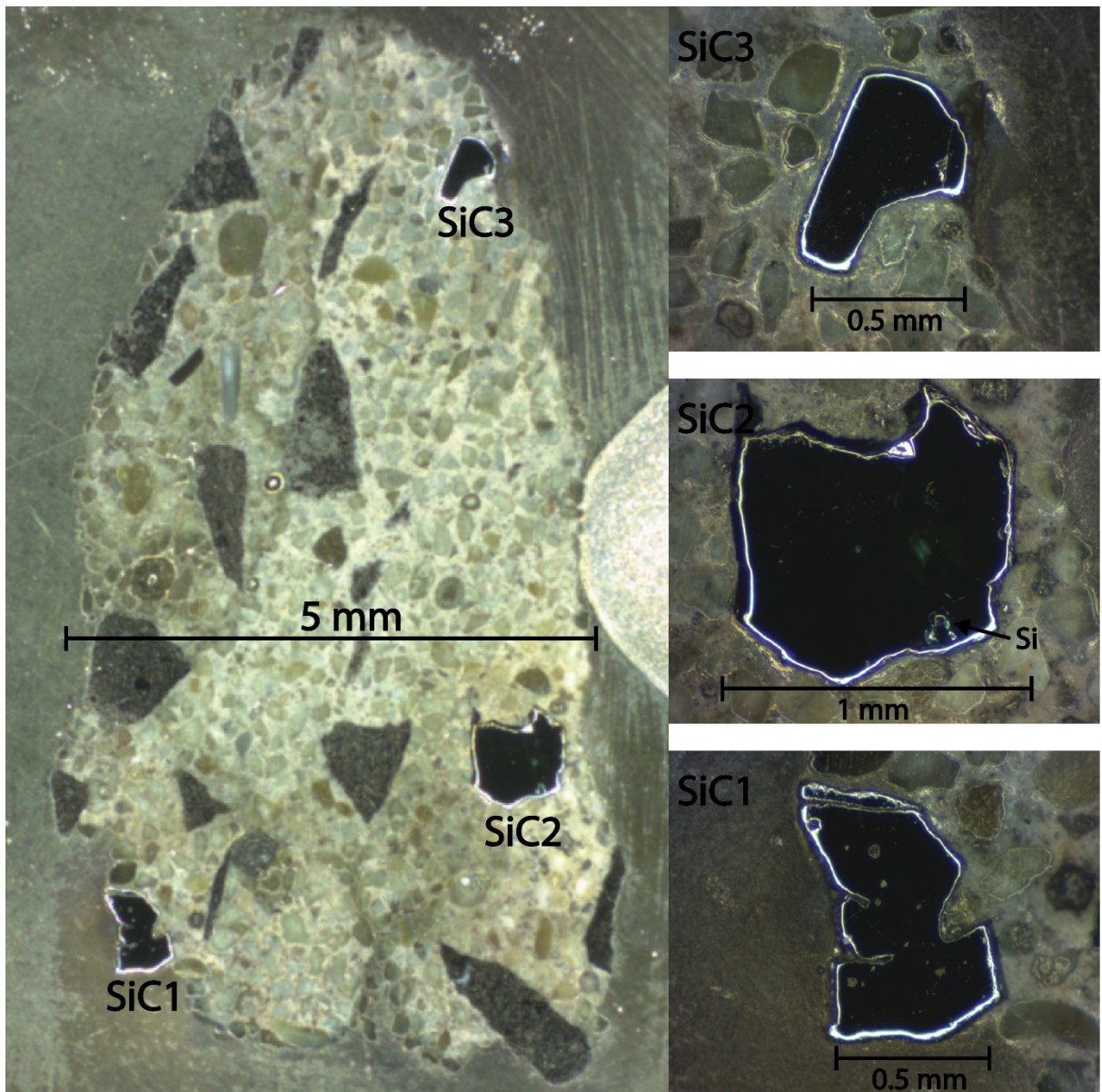
472

473 **Figure 1** The stacking in the 3C-, 6H- and 4H-SiC structures can be interpreted through the orientation of alternating

474 Si and C layers. The unit cell in each case is represented by a dashed line. The layers are labelled based on relative

475 stacking position and depth coming out of the page.

476

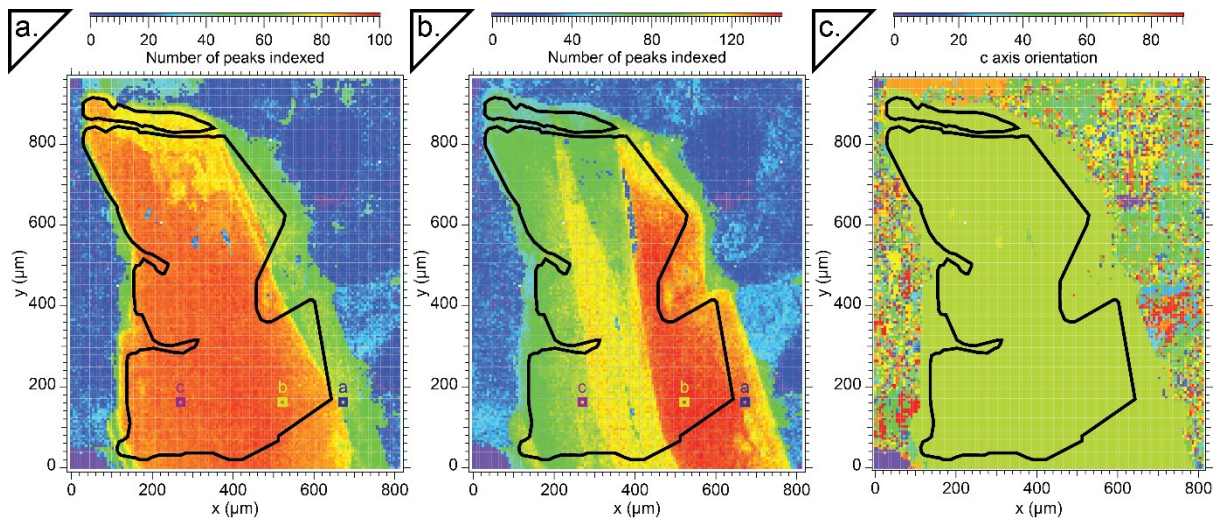


477

478 **Figure 2** The microscope image of the sample clearly shows the location of the SiC grains, which have different

479 reflectivities from the surrounding rock matrix. Location of SiC and the Si inclusion in SiC2 are pointed out.

480



481

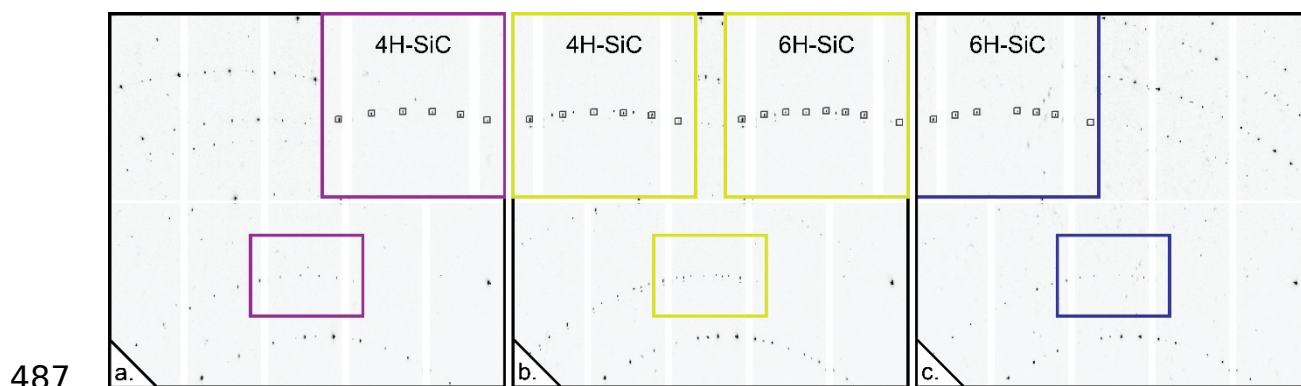
482 **Figure 3** The SiC₁ grain can be indexed as both (a) 4H-SiC and (b) 6H-SiC. (c) c-axis orientation with respect to the

483 sample normal is also shown, to demonstrate the intergrowth of the two crystal types along the same stacking direction.

484 The black outline indicates the surface expression of the sample, based on microscopy images. The squares labelled a, b,

485 and c correspond to the diffraction pattern locations from Figure 4.

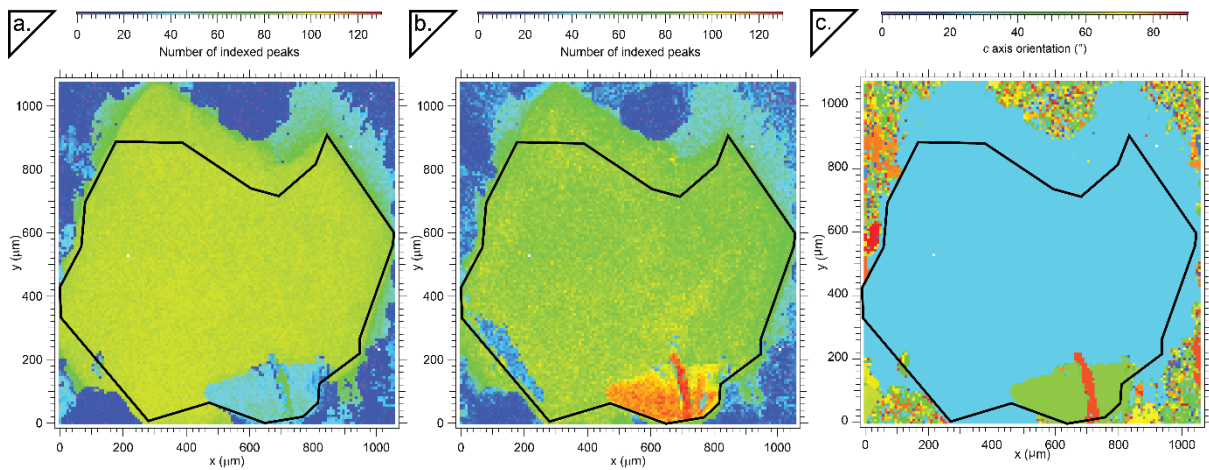
486



487

488 **Figure 4** Diffraction patterns from SiC1 can be indexed as either the 4H- or 6H-SiC. a. This part of the sample indexes
489 solely as 4H-SiC. The inset shows squares around all successfully identified peaks. No additional peaks remain.
490 This area can be indexed as both 4H- and 6H-SiC. The two insets show that all peaks are identified as being part of one or the
491 other stacking type.

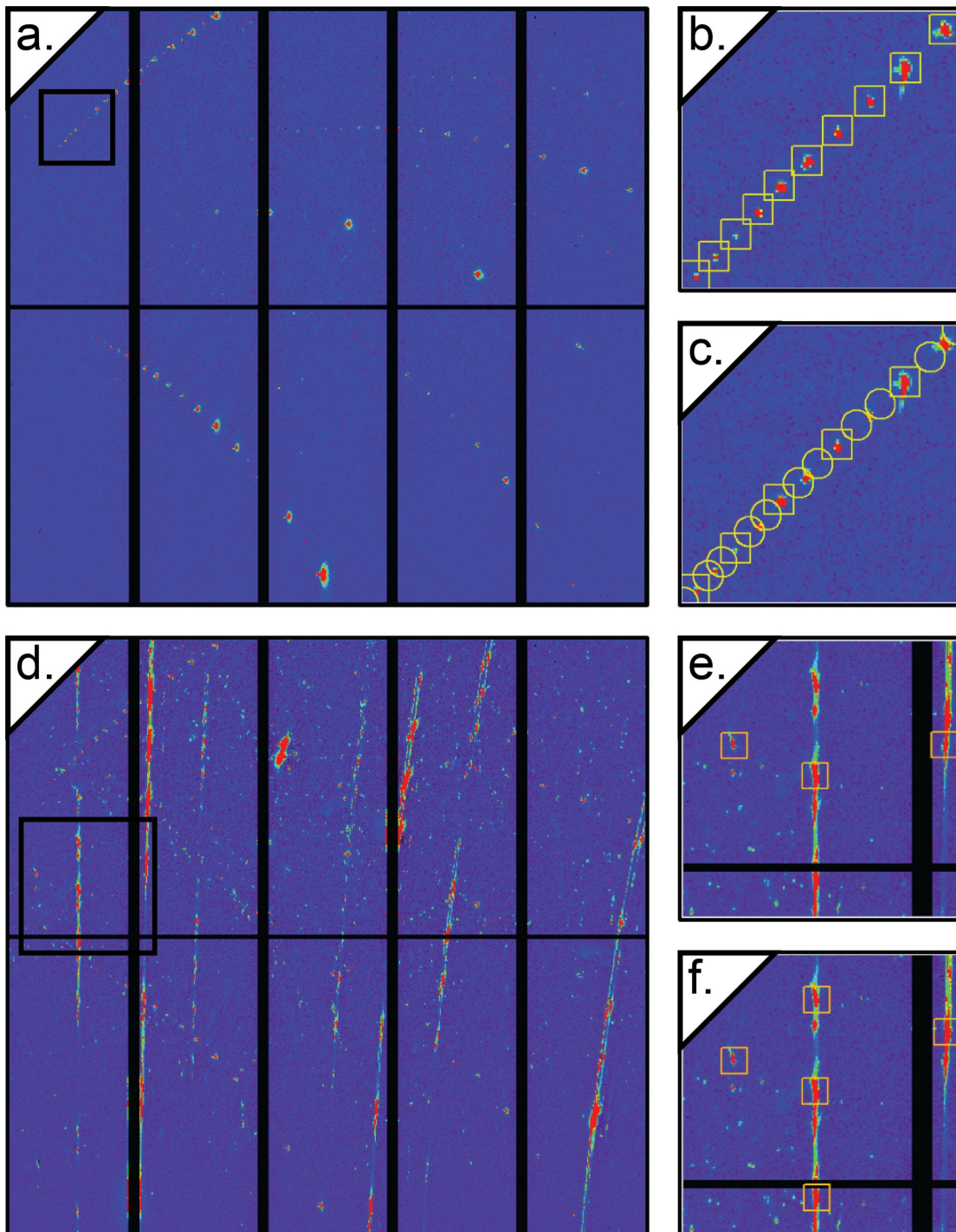
492



493

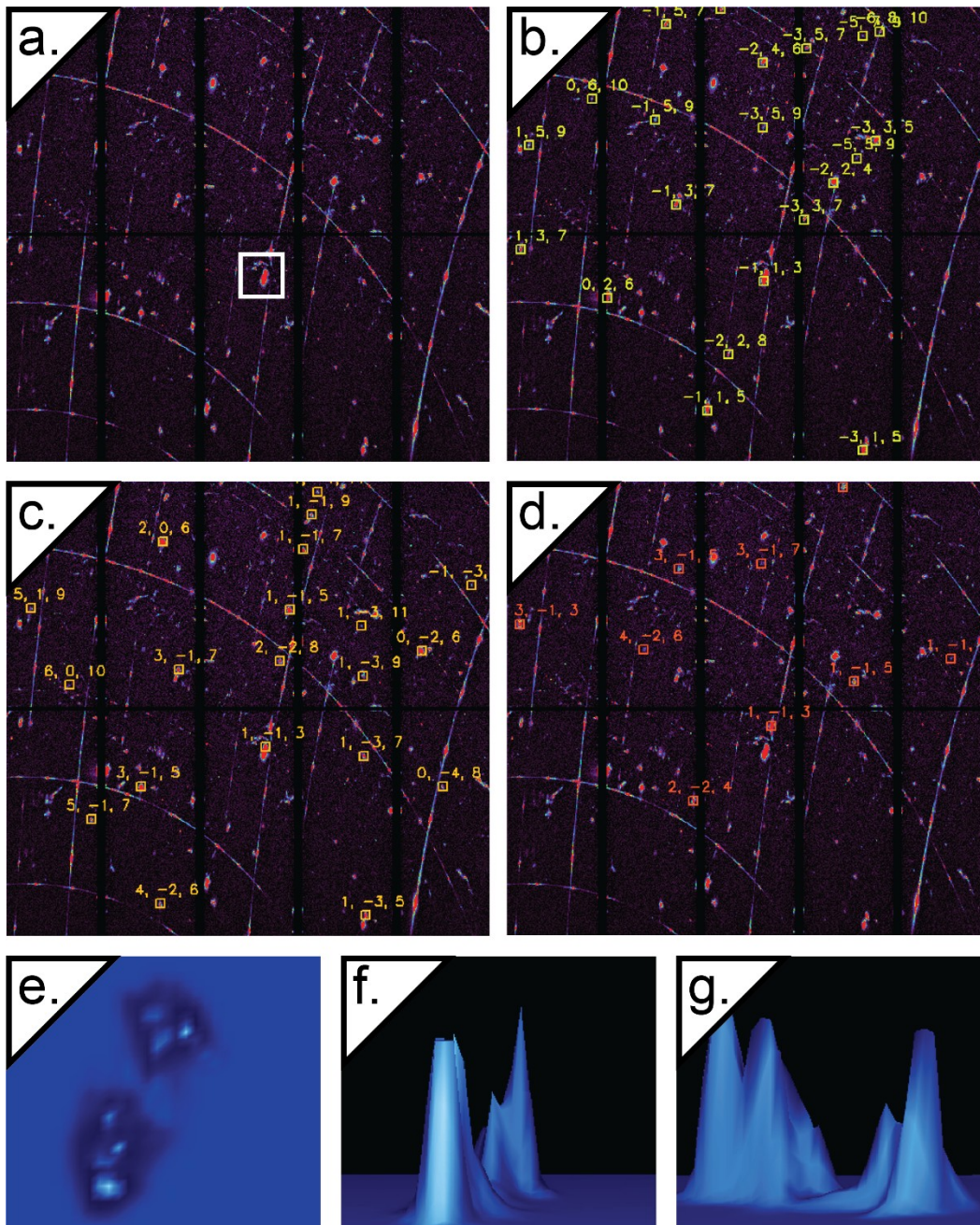
494 **Figure 5** The SiC₂ grain indexed as a. 4H-SiC and b. 6H-SiC. c. The c-axis orientation with respect to the sample
495 normal shows several different orientations are present in this sample. The black outline indicates the surface expression
496 of the sample, based on microscopy images.

497



498

499 **Figure 6** a. This pattern is representative of the SiC₂ sample in the 4H-SiC-indexed region. b. The yellow squares
 500 indicate peaks that were identified and indexed as 4H-SiC. All peaks can be fit with this unit cell. c. The same pattern
 501 from a. is indexed as 6H-SiC. The yellow circles show peaks that are predicted to occur but are not found (with signal-to-
 502 noise ratio > 5). d. This pattern is representative of the polycrystalline region of the SiC₂ sample. e. and f. are
 503 representative fits to the 4H- and 6H-SiC unit cells, respectively. Boxes in a. and d. outline enlarged areas from b., c., d.,
 504 and f.



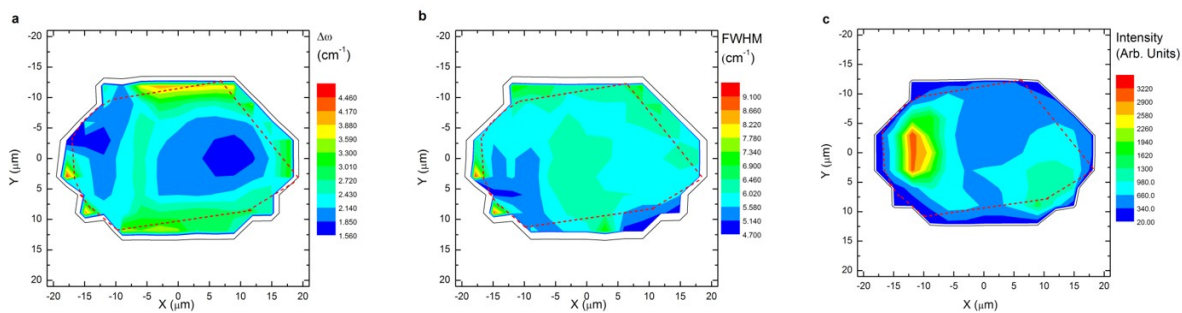
505

506 **Figure 7** a. This is a representative pattern taken in the region of exposed Si inclusion. b., c., and d. show indexation507 fits for three different Si orientations (~33.5, 15.5, and 24.8 degree *c*-axis orientation with respect to sample normal,

508 respectively). e. This is a magnified view of the {113} reflection outlined by a white box in a. f. and g. show 3D

509 projections of the peaks from e. in vertical and horizontal transects, respectively.

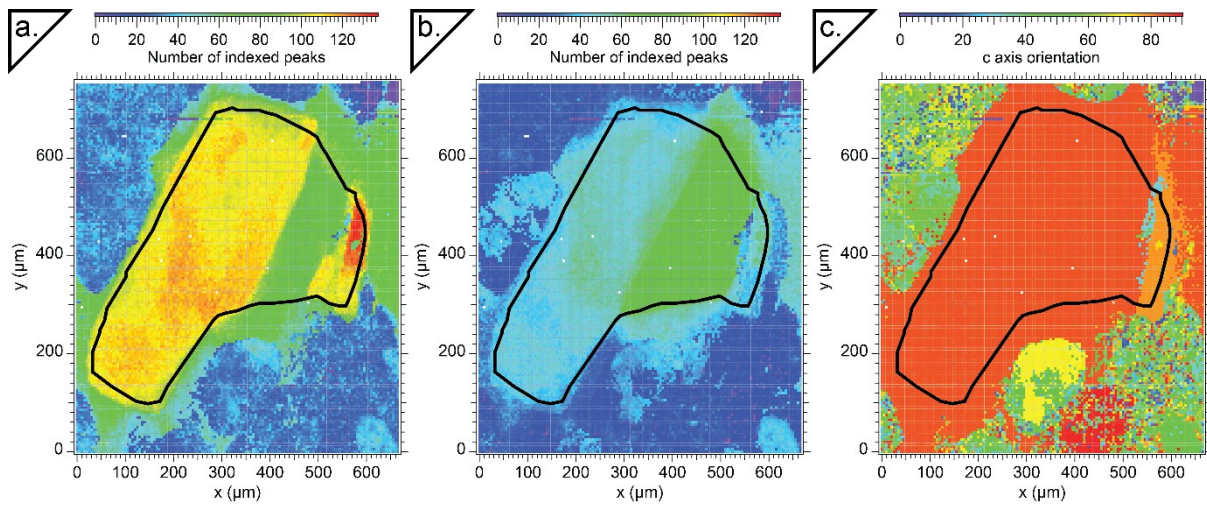
510



511

512 **Figure 8** Raman maps of the Si inclusion. a. $\Delta\omega = \omega_{\text{observed}} - \omega_{\text{unstrained Si}}$. A value of 520.7 cm^{-1} was used for the
 513 unstrained Si. b. Full width at half maximum (FWHM) of the first order Si Raman mode. c. Intensity of the first order Si
 514 Raman mode. The red dashed line outlines the surface expression of the Si inclusion.

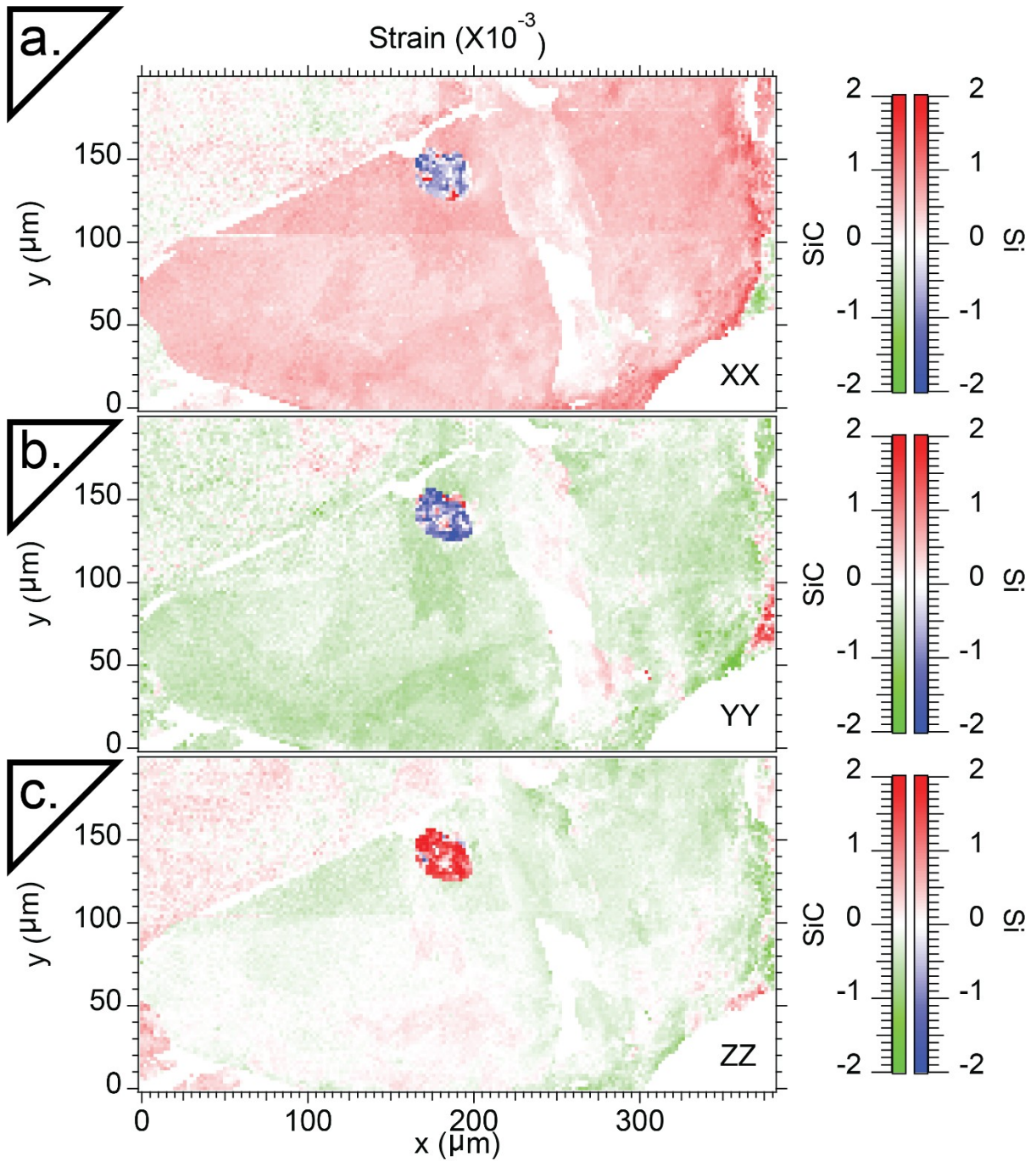
515



516

517 **Figure 9** The SiC₃ grain indexed as a. 6H-SiC and b. 4H-SiC. c. The c-axis orientation with respect to the sample
518 normal shows several different orientations are present in this sample. The black outline indicates the surface expression
519 of the sample, based on microscopy images.

520

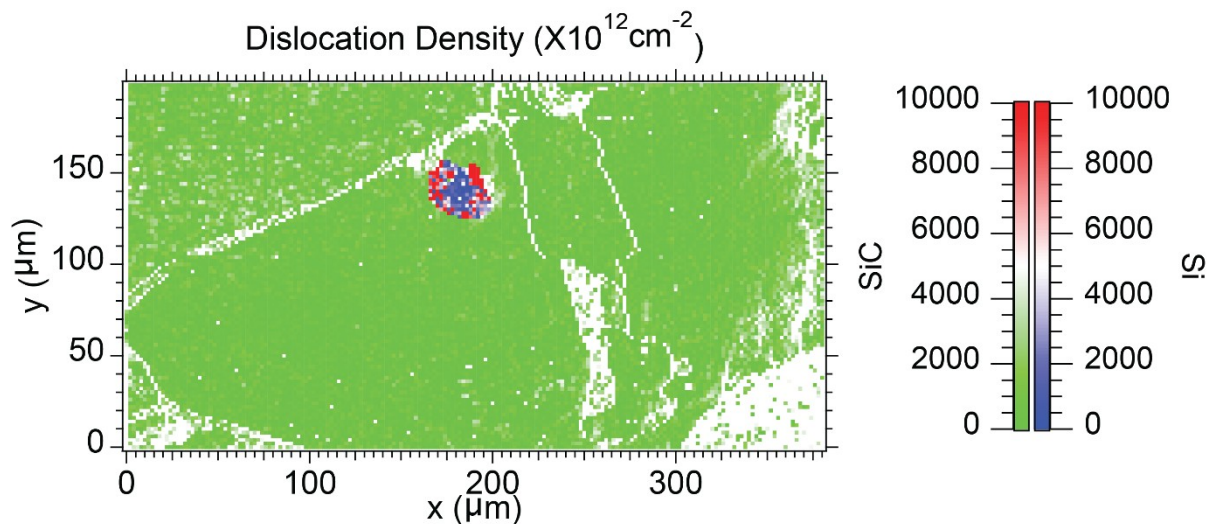


521

522 **Figure 10** Strain maps of the mixed 4H-/6H-SiC region and Si inclusion in the (a) x (horizontal) (b) y (vertical) and (c)

523 z (out of plane) directions.

524



525

526 **Figure 11** Geometrically necessary dislocation density of the mixed 4H-/6H-SiC region and Si inclusion. Notably the
 527 dislocation density of the Si inclusion is high at the edges and low in the middle and the SiC grain shows a very low
 528 dislocation density.

529

530

531 **Table 1** Measurement conditions for microdiffraction. This is a table heading (style: IUCr table caption; this style
532 applies table numbering). Please use the **IUCr tables** (toolbar button) to create experimental and geometry tables when
533 reporting crystal structure data.

534 This is a table headnote (style: IUCr table headnote)

Grain	Map dimensions (μm^2)	Pixel dimension (μm)
SiC1	798 x 972	6
SiC2	1064 x 1080	8
SiC2 ^a	382 x 202	2
SiC3	665 x 755	5

535 ^athe second map was performed over the area where Si was present

536



© 2020 by the authors. Submitted for possible open access publication under the terms and conditions of the Creative Commons Attribution (CC BY) license (<http://creativecommons.org/licenses/by/4.0/>).

537